

inferred angles will remain constant. Consequently, we can predict the future evolution of both the orbital light curve and the pulse profile of A. Given the inferred values of λ , ϕ , ρ , α and δ together with a value of ϕ at a specified time, the five constraint equations determine the pulse profile parameters, P_i and P_o , and the orbital light curve parameters, O_o , O_i and O_m . Both O_i and O_o will remain constant, while O_m , which is equal to ϕ , will increase at a rate of 4.77° per year. This effect will be easily measurable over the next 1–2 years. The geodetic precession will also cause highly significant pulse profile changes over timescales of a few years (see Fig. 3). Note that similar (although smaller-amplitude) precession-induced profile changes have already been observed in the binary system PSR B1913+16^{7,8}. For solution 1, P_o and P_i will increase by $42^\circ \pm 16^\circ$ and $31^\circ \pm 8^\circ$ in 1 year, respectively. For solution 2, P_o and P_i will increase by $96^\circ \pm 13^\circ$ and $34^\circ \pm 6^\circ$ in 1 year, respectively. For both solutions, P_o will approach its maximum extent, 360° , in less than 2 years. Pulsar A is expected to disappear in about 14 years, according to solution 1. According to solution 2, the pulsar will disappear in approximately 4.5 years, and then reappear in 10 years as a single-peaked pulsar (temporarily), where it will remain 'on' for 6–7 years. For both solutions, we estimate that the pulsar came into view approximately 4–5 years in the past. This can explain why the Parkes 70-cm survey for pulsars, completed in 1997, did not detect this system in spite of sufficient sensitivity and appropriate sky coverage⁹.

Recently, Demorest *et al.*¹⁰ used the polarization properties of A together with the standard rotating vector model of ref. 11 in an attempt to measure its emission geometry. Owing to limitations in both the model and the data, they were only able to measure the angle α , which they found to be $4^\circ \pm 3^\circ$. This result is consistent with our solution 1. As they measured only one of the five angles needed to completely specify the geometry, they were unable to predict the future evolution of the emission properties of this system.

We note that the current form of the model does not consider the precession of B. However, it is likely that wind-torques from A, the pulsar that dominates the system energetically, have caused the spin axis of B to align with the direction of the orbital angular momentum^{12,13}. In this case, geodetic precession will have no effect on the emission from B. It is also possible that the direction of B's emission beam may lie in the orbital plane as a result of the stimulated emission process regardless of the magnetic field alignment. In this scenario, geodetic precession would also have little effect on the direction of B's emission.

Given that the model presented here accurately describes the current data, it becomes important to understand the physics behind the stimulation process. Future work will explore various possible mechanisms. One idea involves 'jump-starting' the pulsar emission processes in B by initiating electron–positron pair cascades in its magnetosphere that emit coherent radio emission. The initiating particles could be the positrons and electrons emitted in the wind of A, or, more likely, γ -rays that are expected to be travelling in nearly the same direction as the radio photons. Alternatively, pressure from a conal A-wind could distort B's magnetosphere¹³ and push its beam more directly into our line of sight. □

Received 6 February; accepted 23 February 2004; doi:10.1038/nature02509.

1. Burgay, M. *et al.* An increased estimate of the merger of double neutron stars from observations of a highly relativistic system. *Nature* **426**, 521–533 (2004).
2. Lyne, A. G. *et al.* A double-pulsar system—A rare laboratory for relativistic gravity and plasma physics. *Science* **303**, 1153–1157 (2004).
3. Lyne, A. G. & Manchester, R. N. The shape of pulsar radio beams. *Mon. Not. R. Astron. Soc.* **234**, 477–508 (1988).
4. Ransom, S. *et al.* Green Bank Telescope measurement of the systemic velocity of the double pulsar binary J0737–3039 and implications for its formation. *Astrophys. J.* (submitted); preprint at (<http://xxx.lanl.gov/astro-ph/0404149>) (2004).
5. Barker, B. M. & O'Connell, R. F. Gravitational two-body problem with arbitrary masses, spins, and quadrupole moments. *Phys. Rev. D* **12**, 329–335 (1975).

6. Barker, B. M. & O'Connell, R. F. Relativistic effects in the binary pulsar PSR 1913+16. *Astrophys. J.* **199**, L25–L26 (1975).
7. Kramer, M. Determination of the geometry of the PSR B1913+16 system by geodetic precession. *Astrophys. J.* **509**, 856–860 (1998).
8. Weisberg, J. M. & Taylor, J. H. General relativistic geodetic spin precession in binary pulsar B1913+16: Mapping the emission beam in two dimensions. *Astrophys. J.* **576**, 942–949 (2002).
9. Lyne, A. G. *et al.* The Parkes Southern Pulsar Survey—II. Final results and population analysis. *Mon. Not. R. Astron. Soc.* **295**, 743–755 (1998).
10. Demorest, P. *et al.* Orientations of spin and magnetic dipole axes of pulsars in the J0737–3039 binary based on polarimetry observations at the Green Bank Telescope. *Astrophys. J.* (submitted); preprint at (<http://xxx.lanl.gov/astro-ph/0402025>) (2004).
11. Radhakrishnan, V. & Cooke, D. J. Magnetic poles and the polarization structure of pulsar radiation. *Astrophys. J.* **3**, L225–L228 (1969).
12. Kaspi, V. M. *et al.* Green Bank Telescope observations of the eclipse of pulsar B in the double pulsar binary PSR J0737–3039. *Astrophys. J.* (submitted); preprint at (<http://xxx.lanl.gov/astro-ph/0401614>) (2004).
13. Arons, J., Spitkovskiy, A., Backer, D. & Kaspi, V. Probing relativistic winds and magnetospheres: Torques and eclipses of PSR J0737–3039 A & B. *Astrophys. J.* (submitted).
14. Press, W. H., Flannery, B. P., Teukolsky, S. A. & Vetterling, W. T. *Numerical Recipes in C. The Art of Scientific Computing* (Cambridge Univ. Press, Cambridge, 1988).

Acknowledgements Part of this research was performed at the Jet Propulsion Laboratory, California Institute of Technology, under contract with NASA and funded through the internal Research and Technology Development program. We thank V. Kaspi, J. Armstrong, J. Arons, D. Backer, P. Freire and R. Manchester for discussions and comments. F. J. extends special thanks to T. A. Prince and E. B. Dussan V.

Competing interests statement The authors declare that they have no competing financial interests

Correspondence and requests for materials should be addressed to F.J. (merlyn@alum.mit.edu).

Stardust silicates from primitive meteorites

Kazuhide Nagashima¹, Alexander N. Krot² & Hisayoshi Yurimoto¹

¹Department of Earth and Planetary Sciences, Tokyo Institute of Technology, Ookayama, Meguro, Tokyo 152-8551, Japan

²Hawaii Institute of Geophysics and Planetology, School of Ocean and Earth Science and Technology, University of Hawaii at Manoa, Honolulu, Hawaii 96822, USA

Primitive chondritic meteorites contain material (presolar grains¹), at the level of a few parts per million, that predates the formation of our Solar System. Astronomical observations² and the chemical composition of the Sun³ both suggest that silicates must have been the dominant solids in the protoplanetary disk from which the planets of the Solar System formed, but no presolar silicates have been identified in chondrites^{4–6}. Here we report the *in situ* discovery of presolar silicate grains 0.1–1 μm in size in the matrices of two primitive carbonaceous chondrites. These grains are highly enriched in ¹⁷O ($\delta^{17}\text{O}_{\text{SMOW}} > 100\text{--}400\text{‰}$), but have solar silicon isotopic compositions within analytical uncertainties, suggesting an origin in an oxygen-rich red giant or an asymptotic giant branch star^{7,8}. The estimated abundance of these presolar silicates (3–30 parts per million) is higher than reported for other types of presolar grains in meteorites¹, consistent with their ubiquity in the early Solar System, but is about two orders of magnitude lower than their abundance in anhydrous interplanetary dust particles⁹. This result is best explained by the destruction of silicates during high-temperature processing in the solar nebula.

Acer 094 is a unique, primitive, type 3 carbonaceous chondrite that contains higher abundances of presolar SiC and diamond, and amorphous matrix material, than any other chondrites^{10,11}. North West Africa (NWA) 530 is a CR2 (Renazzo-type) carbonaceous chondrite that experienced very mild aqueous alteration, but escaped

Table 1 Characteristics of presolar silicates and oxides

Grain	Mineral	Size (nm)	$\delta^{17}\text{O}$ (‰)	$\delta^{18}\text{O}$ (‰)	$\delta^{29}\text{Si}$ (‰)	$\delta^{30}\text{Si}$ (‰)
Acfcr 094						
A1028-3	Olivine (Fo ₈₅)	1,000	78.4 (10.3)	-33.5 (5.1)	-9 (14)	3 (14)
A1028-4	Silicate*	100–200	140.7 (10.0)	9.0 (4.8)	-21 (18)	23 (19)
A1119-1	Cor/hib	200	277.2 (10.9)	-71.7 (5.9)	-	-
A1119-3	Silicate*	100–200	311.7 (10.6)	-18.7 (5.6)	-15 (23)	-17 (24)
NWA 530						
N1128-2	Silicate†	100–200	313.5 (10.6)	8.8 (5.7)	-12 (27)	-33 (28)
N1128-4	Silicate†	100–200	85.8 (11.1)	12.0 (5.3)	11 (25)	-7 (26)
N1203-3	Silicate†	100–200	84.1 (10.4)	0.9 (5.3)	-24 (25)	10 (26)

The presolar material was located in the Acfer 094 and NWA 530 matrices, and properties were determined by *in situ* measurements. Isotope ratios correspond to lower limits of true anomalies of the grains owing to dilution effects of isotopography (see Fig. 2 legend). In parenthesis are 1σ errors. Cor, corundum; hib, hibonite.

*Mineralogically similar to the Acfer 094 matrix, composed largely of amorphous material, forsterite and enstatite¹¹.

†Aggregates of several unidentified silicate grains.

thermal metamorphism¹². To search for presolar silicates in these meteorites, high-precision isotope imaging—isotopography—was conducted using a TiTech isotope microscope system (Cameca ims-1270 + SCAPS¹³) following procedures described in ref. 14.

Nine matrix regions of total area 44,100 μm^2 were analysed in each meteorite. In $\delta^{17,18}\text{O}$ isotopographs, candidates for presolar silicates appear as ‘hotspots’ (of warm (red) or cold (blue) colours; Fig. 1). The selection criterion for distinguishing presolar grains is that one of their isotopic ratios is $>2\sigma$ away from the 3σ ellipse of the distribution of the isotopically normal matrix. The errors of hotspots are estimated by the isotopic variations at the peak tops in the isotopographs. Using this criterion, four grains from Acfer 094 and three grains from NWA 530 were determined to be presolar (Table 1, Fig. 2). Because of dilution effects of the surrounding isotopically normal matrix materials (see Fig. 2 legend), the measured isotopic ratios of each presolar grain represent the lower limits of the true isotopic anomalies.

High oxygen ion intensities of the hotspots indicate that all presolar grains detected are silicates and oxides. The mineral identification of the presolar grains is difficult, because the surrounding

matrix material is largely composed of silicate and oxide grains 0.1–0.2 μm in size, which is one-fifth to one-tenth of the lateral resolution of the isotopic and elemental maps. As a result, although ambiguity of the presolar grain identification cannot be completely removed, we were able in most cases to distinguish between silicates and oxides.

Grain A1028-3, $\sim 1 \mu\text{m}$ in size, analysed by electron probe X-ray energy-dispersive spectroscopy (EDS), is a magnesian olivine ($\sim 85 \text{ mol\%}$ forsterite component; Fo_{~85}) of platy morphology, which may be indicative of condensation origin (Fig. 3a). Grain A1119-1, $\sim 0.2 \mu\text{m}$ in size, corresponds to either corundum (Al_2O_3) or hibonite ($\text{CaAl}_{12}\text{O}_{19}$) (Fig. 3b). Five other hotspots correspond to aggregates of 0.1–0.2- μm unidentified silicates (for example, Fig. 3c and d). Because the matrices around these five hotspots are not petrographically different from the presolar grain-free matrix areas largely composed of amorphous material, forsterite (Mg_2SiO_4) and enstatite (MgSiO_3)¹¹, we infer that the unidentified presolar silicates in Acfer 094 (A1028-4 and A1119-3) and in NWA 530 (N1128-2, N1128-4 and N1203-3) could be any of these phases. However, we cannot exclude a possibility of misidentification if very small ($<50 \text{ nm}$) presolar oxide grains are embedded within the silicate clusters. To distinguish between these alternatives, nanoscale isotopic and mineralogical analyses are required. The size ranges of presolar silicates in this study (0.1–1 μm) are essentially equivalent to those of anhydrous interplanetary dust particles (IDPs; 0.3–0.9 μm , ref. 9).

The presolar grains in Acfer 094 and NWA 530 are highly enriched in ^{17}O compared with the solar composition, and have solar or slightly depleted ^{18}O (Fig. 2). These characteristics fall within the range of O isotopic compositions of presolar silicate grains in anhydrous IDPs⁹, and correspond to the group 1 category of presolar oxide grains in meteorites⁷, suggesting an origin in O-rich red giant and asymptotic giant branch (AGB) stars⁷. The silicon isotopic compositions of the presolar silicates are within analytical errors (2σ) of the solar compositions (Table 1). These results indicate that the degree of Si isotope anomalies are smaller

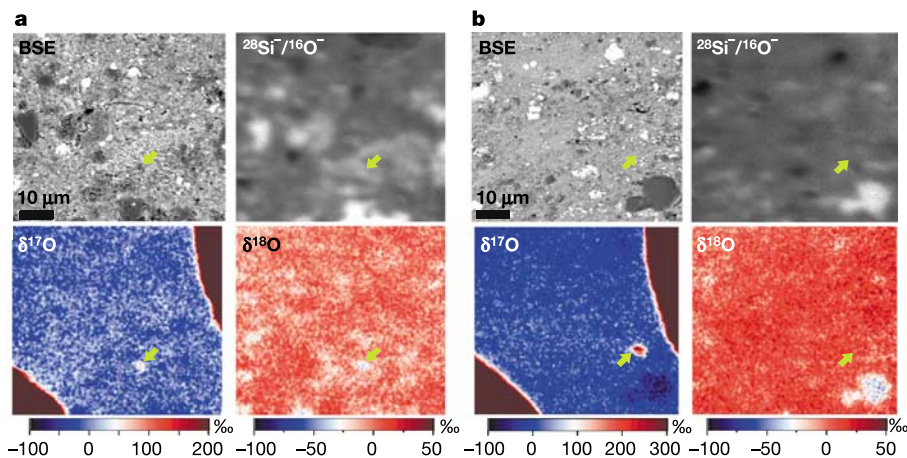


Figure 1 Corresponding images of backscattered electrons, secondary ion ratio ($^{28}\text{Si}^-/^{16}\text{O}^-$), and oxygen isotope ratios ($\delta^{17}\text{O}$ and $\delta^{18}\text{O}$) of matrices. **a**, Acfer 094; **b**, NWA 530. The lateral resolution of the isotopographs is defined with respect to a junction between two distinct phases; it is given by the horizontal distance over which the intensity drops from 84% to 16% of maximum signal (equivalent to 2σ of the error curve); we obtain values of $\sim 1 \mu\text{m}$. The typical sequence for acquiring isotopographs was $^{27}\text{Al}^-$, $^{28}\text{Si}^-$, $^{29}\text{Si}^-$, $^{30}\text{Si}^-$, $^{28}\text{Si}^-$, $^{16}\text{O}^-$, $^{18}\text{O}^-$, $^{16}\text{O}^-$, $^{17}\text{O}^-$, $^{16}\text{O}^-$, $^{12}\text{C}^-$, $^{13}\text{C}^-$ and $^{12}\text{C}^-$. The sputtering depth during the sequence ($\sim 1.5 \text{ h}$) was less than 100 nm. For oxygen isotopographs, values of $\delta^{17,18}\text{O}$ normalized to the SMOW (standard mean ocean water) scale were calculated from secondary ion intensity ratios for each pixel, assuming that the average values of the matrix areas in the isotopograph correspond to those reported^{22,23}, and are displayed by false colour:

$\delta^{17,18}\text{O}_{\text{sample}} (\text{‰}) = \left\{ \left(\frac{^{17,18}\text{R}_{\text{sample}}}{^{17,18}\text{R}_{\text{SMOW}}} - 1 \right) \times 1,000 \right\}$, where $^{17,18}\text{R}$ is an oxygen isotope ratio relative to ^{16}O , and ‘sample’ corresponds to a pixel in the image. The digital image processing using a moving average with 5×5 pixels was applied to simple $\delta^{17,18}\text{O}$ isotopographs in order to reduce the statistical error. Yellow arrows indicate locations of presolar grains A1028-3 (**a**) and N1128-2 (**b**). Reddish brown areas at upper right and lower left corners of $\delta^{17}\text{O}$ images show interference by $^{16}\text{OH}^-$. Typical errors (3σ) of isotopographs for $\delta^{17}\text{O}$ (40‰) and $\delta^{18}\text{O}$ (15‰) are much smaller than those obtained by conventional methods of imaging^{7,9}. Such high precision allows recognition of micro-sized refractory inclusions in $\delta^{17,18}\text{O}$ isotopographs. Major mottled patterns of $\delta^{18}\text{O}$ are not analytical artefacts, but correspond to distributions of small refractory inclusions. Note the good correspondence between $\delta^{17}\text{O}$ and $\delta^{18}\text{O}$, indicating ^{16}O enrichment of about -40‰ (for example, an amoeboid olivine aggregate near the lower right corner of **b**).

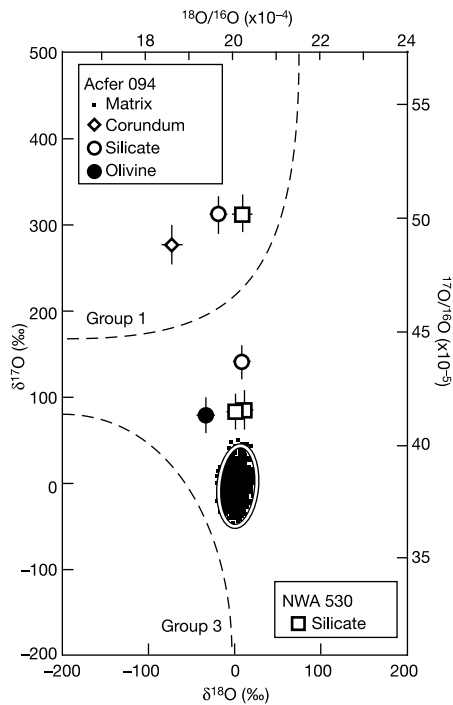


Figure 2 Oxygen isotopic ratios of presolar silicate and oxide grains. Data from Acfer 094 and NWA 530 carbonaceous chondrites. Also shown are the isotopic ratios of matrix materials having isotopically normal (solar) values and the boundaries of presolar oxides of groups 1 and 3 (ref. 7). The error ellipse around the matrix compositions has axes that are 3σ in the direction of the correlation line for the matrix and normal to it. Error bars for presolar grains denote 2σ . Because the lateral resolution of an isotopograph is limited to $\sim 1\ \mu\text{m}$, if the isotopically anomalous grains are smaller than $1\ \mu\text{m}$ then the isotopically anomalous values will be diluted by the surrounding grains having isotopically normal (solar) composition. For example, if the secondary ions in a pixel are averaged in a minimum area of lateral resolution ($1 \times 1\ \mu\text{m}$) and the total secondary ions of three O isotopes are homogeneously emitted in the area, the identification limits of isotope anomalies defined by 3σ criteria are 160‰ and $4,000\text{‰}$ for $\delta^{17}\text{O}$, and 60‰ and $1,500\text{‰}$ for $\delta^{18}\text{O}$, for grains of 0.5 and $0.1\ \mu\text{m}$ in size, respectively. This approximation seems to be appropriate if the area consists of silicate and oxide minerals, which account for $>90\%$ of the matrix. According to this estimated dilution effect, all presolar grains observed in IDPs⁹ can be detected under the analytical condition of isotopography. In the case of Si isotopes, typical errors (3σ) for $\delta^{29}\text{Si}$ and $\delta^{30}\text{Si}$ isotopography are estimated to 60‰ and 70‰ , respectively. The identification limits (3σ) of $\delta^{29}\text{Si}$ and $\delta^{30}\text{Si}$ are estimated to be 240‰ and 280‰ for $0.5\ \mu\text{m}$ grains, and $6,000\text{‰}$ and $7,000\text{‰}$ for $0.1\ \mu\text{m}$ grains, respectively.

than those of O. The smaller Si isotope anomalies compared with those of O are consistent with the origin of presolar silicates from red giant and AGB stars; similar characteristics are observed in presolar SiC from C-rich AGB stars¹⁵.

The grain densities of presolar silicates in the matrices of Acfer 094 and NWA 530 are similar (~ 85 per mm^2); the calculated abundances in the matrix are 30 parts per million (p.p.m.) and 3 p.p.m., respectively. The larger abundance of presolar silicates in Acfer 094 is due to the existence of one large ($1\text{-}\mu\text{m}$ -sized) presolar olivine, and is not statistically significant. The abundance of presolar silicates in chondritic matrices is comparable to, or higher than, the most abundant presolar grains previously reported in meteorites (for example, 14.2 p.p.m. for SiC and 10.3 p.p.m. for graphite in the Orgueil meteorite¹⁶), except for diamond. We note, however, that probably not all diamonds in meteorites are presolar¹⁷. In comparison, the grain density and abundance of presolar silicates in anhydrous cluster IDPs are $\sim 20,000$ per mm^2 and $\sim 5,500$ p.p.m. (ref. 9), respectively.

The lower abundances of presolar silicates in unmetamorphosed

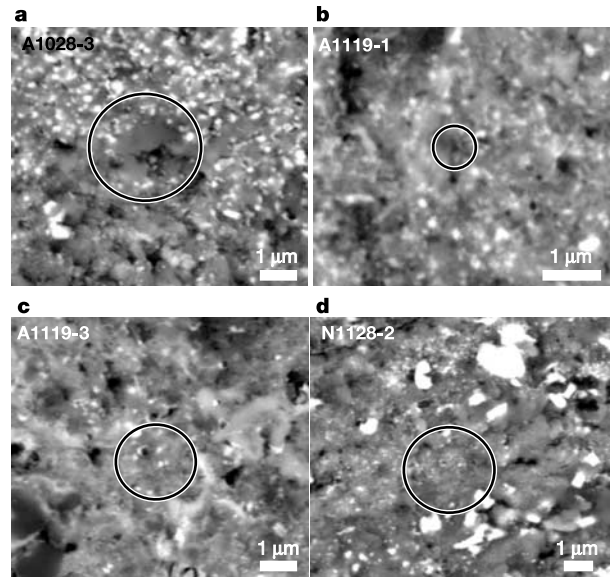


Figure 3 Backscattered electron images of presolar grains embedded in meteorite matrices. **a**, A1028-3, **b**, A1119-1, **c**, A1119-3 from Acfer 094, and **d**, N1128-2 from NWA 530. Mineral characterizations of presolar grains and surrounding matrix materials were conducted by backscattered electron and secondary electron imaging and elemental mapping using a JEOL JSM-5310LV scanning electron microscope with an Oxford LINK-ISIS EDS at TiTech. Quantitative analyses were collected using a focused (diameter $< 1\ \mu\text{m}$) $15\ \text{keV}$, $1\ \text{nA}$ beam and 100-s counting time. Quantitative corrections were applied using a ZAF software routine. For electron imaging and elemental mapping, a focused electron beam in the range $5\text{--}15\ \text{keV}$ was selected to adjust higher lateral resolution images/maps of the system. X-ray spectrum patterns were also used to identify mineral phases of submicrometre grains. Circles correspond to the locations of oxygen isotope anomalies. A1028-3 and A1119-1 are an olivine grain and either a corundum or a hibonite grain embedded in fine-grained matrix, respectively. No distinguishable grain can be identified in the circle for A1119-3 and N1128-2, but the circle areas consist of silicate clusters.

chondrite matrices compared with IDPs could be due to grain destruction during thermal processing of matrix materials either in the solar nebula (for example, by evaporation–recondensation) or on the parent asteroids (for example, by aqueous alteration). Because during aqueous alteration, smaller grains are expected to be preferentially destroyed, the size distribution of presolar grains before and after alteration should be different. The similar size ranges of presolar silicate grains in meteorite matrices and in anhydrous IDPs, and the lack of aqueous alteration effects in Acfer 094 appear to be inconsistent with destruction of presolar silicates on a parent asteroid.

The chondrite parent asteroids are believed to have formed in the inner solar nebula ($\sim 1\text{--}3\ \text{AU}$). Although both comets and asteroids contribute IDPs to the Earth and the relative fractions of IDPs from each are still not well determined¹⁸, some anhydrous IDPs probably have a cometary origin and represent the outer regions ($5\text{--}55\ \text{AU}$) of the solar nebula¹⁹. We infer that the observed differences in presolar silicate grain abundances in the chondrite matrices and anhydrous IDPs must have resulted from high-temperature nebular processes (for example, chondrule and refractory inclusion formation), which were more effective in the inner parts of the solar nebula^{20,21}. □

Received 16 February; accepted 23 March 2004; doi:10.1038/nature02510.

- Nittler, L. R. Presolar stardust in meteorites: recent advances and scientific frontiers. *Earth Planet. Sci. Lett.* **209**, 259–273 (2003).
- Waters, L. B. F. M. *et al.* Mineralogy of oxygen-rich dust shells. *Astron. Astrophys.* **315**, L361–L364 (1996).
- Anders, E. & Grevesse, N. Abundances of the elements: meteoritic and solar. *Geochim. Cosmochim. Acta* **53**, 197–214 (1989).

4. Messenger, S. & Bernatowicz, T. J. Search for presolar silicates in Acfer 094. *Meteorit. Planet. Sci.* **35**, A109 (2000).
5. Alexander, C. M. O'D., Nittler, L. R. & Tera, F. The search of presolar silicates and the ^{54}Cr carrier. *Lunar Planet. Sci.* [CD-ROM] XXXII, 2191 (2001).
6. Mostefaoui, S., Hoppe, P., Marhas, K. K. & Gröner, E. Search for *in situ* presolar oxygen-rich dust in meteorites. *Meteorit. Planet. Sci.* **38**, A99 (2003).
7. Nittler, L. R., Alexander, C. M. O'D., Gao, X., Walker, R. M. & Zinner, E. Stellar sapphires: The properties and origins of presolar Al_2O_3 in meteorites. *Astrophys. J.* **483**, 475–495 (1997).
8. Lugaro, M., Zinner, E., Gallino, R. & Amari, S. Si isotopic ratios in mainstream presolar SiC grains revisited. *Astrophys. J.* **527**, 369–394 (1999).
9. Messenger, S., Keller, L. P., Stadermann, F. J., Walker, R. M. & Zinner, E. Samples of stars beyond the solar system: silicate grains in interplanetary dust. *Science* **300**, 105–108 (2003).
10. Newton, J. *et al.* Acfer 094, a uniquely primitive carbonaceous chondrite from the Sahara. *Meteoritics* **30**, 47–56 (1995).
11. Greshake, A. The primitive matrix components of the unique carbonaceous chondrite Acfer 094: a TEM study. *Geochim. Cosmochim. Acta* **61**, 437–452 (1997).
12. Krot, A. N., Meibom, A., Weisberg, M. K. & Keil, K. The CR chondrite clan: implications for early solar system processes. *Meteorit. Planet. Sci.* **37**, 1451–1490 (2002).
13. Yurimoto, H., Nagashima, K. & Kunihiro, T. High precision isotope micro-imaging of materials. *Appl. Surf. Sci.* **203–204**, 793–797 (2003).
14. Kunihiro, T., Nagashima, K. & Yurimoto, H. Microscopic oxygen isotopic homogeneity/heterogeneity in the matrix from the Vigarano CV3 chondrite. *Geochim. Cosmochim. Acta* (submitted).
15. Hoppe, P. & Ott, U. in *Astrophysical Implications of the Laboratory Study of Presolar Materials* (eds Bernatowicz, T. J. & Zinner, E.) 27–58 (AIP Press, New York, 1997).
16. Huss, G. R., Meshik, A. P., Smith, J. B. & Hohenberg, C. M. Presolar diamond, silicon carbide, and graphite in carbonaceous chondrites: Implications for thermal processing in the solar nebula. *Geochim. Cosmochim. Acta* **67**, 4823–4848 (2003).
17. Dai, Z. R. *et al.* Possible *in situ* formation of meteoritic nanodiamonds in the early Solar System. *Nature* **418**, 157–159 (2002).
18. Jessberger, E. K. *et al.* in *Interplanetary Dust* (eds Grün, E., Gustafson, B. Å. S., Dermott, S. F. & Fechtig, H.) 253–294 (Springer, Berlin, 2001).
19. Bradley, J. P. & Brownlee, D. E. Cometary particles: thin sectioning and electron beam analysis. *Science* **231**, 1542–1544 (1986).
20. Hewins, R. H. in *Chondrules and the Protoplanetary Disk* (eds Hewins, R. H., Jones, R. H. & Scott, E. R. D.) 3–9 (Cambridge Univ. Press, Cambridge, 1996).
21. Itoh, S. & Yurimoto, H. Contemporaneous formation of chondrules and refractory inclusions in the early Solar System. *Nature* **423**, 728–731 (2003).
22. Bischoff, A. *et al.* New carbonaceous and type 3 ordinary chondrites from the Sahara Desert. *Meteoritics* **26**, 318 (1991).
23. Clayton, R. N. & Mayeda, T. K. Oxygen isotope studies of carbonaceous chondrites. *Geochim. Cosmochim. Acta* **63**, 2089–2104 (1999).

Acknowledgements We thank E. R. D. Scott for discussions, and I. Takayanagi, K. Kosaka and Suzushin-Kogyo for assistance with SCAPS development. This work was supported by Monksasho (H.Y.) and NASA (A.N.K.).

Competing interests statement The authors declare that they have no competing financial interests.

Correspondence and requests for materials should be addressed to K.N. (kazu@geo.titech.ac.jp).

Carbon nanotubes as nanoscale mass conveyors

B. C. Regan^{1,3}, S. Aloni^{1,3}, R. O. Ritchie^{3,2}, U. Dahmen^{3,4} & A. Zettl^{1,3}

¹Department of Physics, ²Department of Materials Science and Engineering, University of California at Berkeley, California 94720, USA

³Materials Sciences Division, ⁴National Center for Electron Microscopy, Lawrence Berkeley National Laboratory, Berkeley, California 94720, USA

The development of manipulation tools that are not too ‘fat’ or too ‘sticky’ for atomic scale assembly is an important challenge facing nanotechnology¹. Impressive nanofabrication capabilities have been demonstrated with scanning probe manipulation of atoms^{2–5} and molecules^{4,6} on clean surfaces. However, as fabrication tools, both scanning tunnelling and atomic force microscopes suffer from a loading deficiency: although they can manipulate atoms already present, they cannot efficiently deliver atoms to the work area. Carbon nanotubes, with their hollow cores and large aspect ratios, have been suggested^{7,8} as possible conduits for nanoscale amounts of material. Already much effort

has been devoted to the filling of nanotubes^{8–11} and the application of such techniques^{12,13}. Furthermore, carbon nanotubes have been used as probes in scanning probe microscopy^{14–16}. If the atomic placement and manipulation capability already demonstrated by scanning probe microscopy could be combined with a nanotube delivery system, a formidable nanoassembly tool would result. Here we report the achievement of controllable, reversible atomic scale mass transport along carbon nanotubes, using indium metal as the prototype transport species. This transport process has similarities to conventional electromigration, a phenomenon of critical importance to the semiconductor industry^{17,18}.

Our experiments are performed inside a JEOL-2010 transmission electron microscope (TEM) equipped with a piezo-driven nanomanipulation stage (Nanofactory Instruments AB). Indium metal is thermally evaporated *ex situ* onto a boule of arc-grown multiwalled carbon nanotubes (MWNTs), which decorates the nanotubes with isolated indium nanocrystals¹⁹. The coated boule is then fixed to the sample side of the TEM stage. Inside the TEM, under high vacuum conditions, an individual nanotube or bundle is approached with a freshly etched tungsten tip mounted on the nanomanipulator, and physical contact is made between the tip and the free end of the nanotube. Applying a voltage between the tip and the sample holder establishes an electrical circuit through the subject tube, and injects thermal energy into the system via Joule heating. By increasing the applied voltage, the local temperature can be easily increased past the melting point of the indium particles decorating the tube. Further manipulation of the voltage produces dramatic mass transport between these nanoparticles, which serve as mass reservoirs. The transport process is recorded using real-time TEM video imaging.

Figure 1 gives a series of video frames illustrating the transport process. A single MWNT, clean except for resident indium particles, spans each image from left to right. During the three-minute period shown, a current of $\sim 40\ \mu\text{A}$ is passing through the MWNT. The first frame of Fig. 1 shows three large indium particles, separated by about 100 nm, and several smaller ones. The dark contrast and nearly round shapes indicate that the particles are molten. As the experiment proceeds, particles to the left are generally getting smaller, while those to the right grow. Tracking the central large particle in particular, we see that it grows between the first and second frames—while there are still particles to its left—but shrinks thereafter. Qualitative inspection suggests a near unity correlation

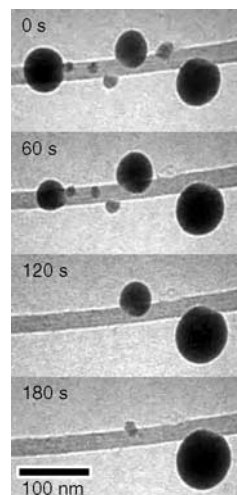


Figure 1 Four TEM video images, spaced by one-minute increments, showing left-to-right indium transport on a single MWNT. The tip (anode) is out of view to the left and the sample electrode (cathode) is out of view to the right. The measured circuit resistance is $\sim 49\ \text{k}\Omega$, most of which is presumably concentrated at the tip–MWNT contact.